RSC Advances

PAPER

View Article Online
View Journal | View Issue

Cite this: *RSC Adv.*, 2025, **15**, 48487

3D coral-like Ni–Mo–S/NF bifunctional electrocatalyst for concurrent glycerol valorization to formate and energy-efficient H_2 evolution

Yong Liu,[ab] Bohon Chen,[ab] Hanbin Nie,[ab] Shuanglin Gui[ab] and Jianping Deng *[ab]

Electrolytic hydrogen production from water is a cost-effective renewable energy technology, but its development is severely constrained by high energy consumption, precious metal catalysts, and low-value products of anode. Given that inexpensive glycerol exhibits a significantly lower redox potential than water, this study developed a 3D coral-like nickel–molybdenum sulfur bifunctional nanocatalyst (Ni–Mo–S/NF) based on nickel foam, which served as both the anode and cathode in an alkaline glycerol electrolyte, enabling the simultaneous production of high-value formate at the anode and high-purity hydrogen at the cathode. Notably, in a two-electrode system, the alkaline glycerol electrolyzer required only 1.37 V to achieve a current density of 10 mA cm^{-2}, which was 280 mV lower than that of an alkaline aqueous solution system, indicating an about 17% reduction in energy consumption compared to conventional water electrolysis. Meanwhile, this system reached a faradaic efficiency of 95.0% for formate production and 99.6% for hydrogen evolution. Benefiting from the outstanding performance of the noble-metal-free Ni–Mo–S/NF catalyst, the proposed technology for simultaneous formate and hydrogen production *via* glycerol electrooxidation offers a novel pathway for the green production of high-value chemicals and energy-saving hydrogen generation.

Received 13th November 2025
Accepted 1st December 2025

DOI: 10.1039/d5ra08754f

rsc.li/rsc-advances

1. Introduction

In today's world marked by rapid technological advancement and escalating climate challenges, the concept of sustainable development and the urgent demand for clean energy technologies have reached a global consensus.[1] Electrocatalytic technology has garnered significant attention as an efficient and environmentally benign approach for energy conversion and storage, particularly in hydrogen production through water electrolysis powered by renewable energy sources such as wind and solar power.[2] In conventional water electrolysis for hydrogen production, the anodic oxygen evolution reaction (OER) exhibits sluggish kinetics and requires high overpotential, resulting in high overall energy consumption.[3,4] Additionally, the low-value oxygen byproduct generated at the anode may mix with cathodic hydrogen, creating potential explosion hazards. Therefore, identifying thermodynamically favorable alternative anode reactions to replace OER has emerged as a key strategy for reducing the energy consumption and safety risks of electrocatalytic hydrogen production.

In recent years, electrocatalytic oxidation of more easily oxidized small molecules (*e.g.*, ammonia, urea and hydroxylamine),[5–7] has been recognized as an effective method for significantly reducing the electrolysis voltage for hydrogen generation, replacing the water splitting reaction. Although the theoretical voltage for water electrolysis is 1.23 V, the actual operating voltage typically ranges from 1.5 to 2.0 V due to reaction energy barriers and could be even higher in commercial electrolyzers.[8,9] In contrast, the operational voltage for these small-molecule electrolysis systems can be substantially lowered to 0.6–1.5 V, with potential for further reduction under optimized conditions, thereby dramatically cutting energy demands.[10] However, since these small molecules solely served as sacrificial agents at the anode, their utilization inevitably increased hydrogen production costs. Glycerol, with a theoretical oxidation potential of only 0.69 V, regarded as an ideal organic molecular alternative, is a low-value byproduct mass-produced in biodiesel manufacturing.[11,12] Beyond enabling reduced cell voltages, its selective electrooxidation simultaneously yields multiple high-value chemicals including glycerate, glycolate, and formate.[13] Among these, formic acid (formate) is particularly noteworthy as both a crucial chemical intermediate and a promising hydrogen energy carrier for fuel cell applications due to its high hydrogen storage capacity.[14] However, conventional industrial production of formic acid involves complex processes and high costs, making the electrochemical oxidation of low-value glycerol to formic acid

[a]*Jiangxi Provincial Key Laboratory of Greenhouse Gas Accounting and Carbon Reduction, Institute of Energy Research, Jiangxi Academy of Sciences, Nanchang 330096, People's Republic of China. E-mail: jpdeng9199@163.com*
[b]*Jiangxi Carbon Neutralization Research Center, Nanchang 330096, People's Republic of China*

an attractive alternative. Therefore, in alkaline electrocatalytic systems, replacing the oxygen evolution reaction (OER) with the glycerol oxidation reaction (GOR) presents a promising low-energy hydrogen production strategy, while simultaneously yielding high-value-added formate.[15,16]

To date, noble metals and their compounds remain the most widely used catalysts for both HER and electro-oxidation reactions, yet their scarcity and high cost severely limit large-scale applications.[17,18] Consequently, the rational design of earth-abundant, cost-effective non-noble metal electrocatalysts exhibiting comparable activity and durability to noble metal benchmarks represents a crucial research direction for sustainable energy conversion.[19,20] Recent studies have reported that transition metal sulfides appeared considerable catalytic activity and stability in electrocatalytic processes such as OER and HER, representing a class of highly promising and application-worthy electrocatalysts.[21] Bi *et al.* successfully synthesized CoS_2/MoS_2 on carbon cloth *via* a facile one-step method,[22] demonstrating exceptional HER performance in 1.0 M KOH with a low overpotential of 73 mV at 10 mA cm^{-2} and a Tafel slope of 80.42 mV dec^{-1}. Xue *et al. in situ* grew nanostructured NiTe/NiS on nickel foam,[23] achieving outstanding OER activity in 1.0 M KOH (overpotential of 257 mV at 100 mA cm^{-2}) with a Tafel slope of 49 mV dec^{-1}. Mechanistic studies revealed that strong electronic interactions at the nano-interfaces induced electronic structure modulation, which optimized the binding energy of OOH^- intermediates and consequently enhanced OER performance. Furthermore, Liu *et al.* developed a Ni_3S_2–FeS/NF catalyst and maintained continuous operation for over 200 hours under industrial conditions (500 mA cm^{-2} at 1.71 V and 70 °C) in an alkaline exchange membrane water electrolyzer,[24] highlighting its strong potential for practical applications. Despite extensive investigations into transition metal sulfides for pure water splitting reactions, their bifunctional capability to simultaneously drive hydrogen evolution and organic valorization (*e.g.*, GOR-to-formate conversion) remains underexplored, creating a critical knowledge gap in sustainable electrochemical energy conversion systems.

Herein, we developed three-dimensional coral-like Ni–Mo–S nanostructured catalysts directly grown on nickel foam (NF) substrates *via* a precisely controlled one-pot hydrothermal method. When configured as both anode and cathode in an alkaline membrane-free electrolyzer of glycerol, this Ni–Mo–S/NF bifunctional electrode system enabled concurrent: (i) anodic glycerol valorization to formate, and (ii) cathodic hydrogen evolution. In this work, the glycerol oxidation reaction (GOR) at the anode successfully replaced the oxygen evolution reaction (OER), producing high-value formate with remarkable faradaic efficiency (95%) and selectivity (86%). Since glycerol is more readily oxidized than water, this system required only 1.31 V to drive hydrogen evolution at 10 mA cm^{-2}, indicating an about 17% reduction in energy consumption compared to conventional water electrolysis. This study achieved simultaneous value-added conversion of chemicals and energy-efficient hydrogen production using transition metal sulfide bifunctional electrocatalysts, representing a highly promising and impactful strategy in sustainable energy research.

2. Experimental section

2.1 Materials and chemicals

Nickel acetate tetrahydrate ($Ni(CH_3COO)_2 \cdot 4H_2O$, 99%), ammonium molybdate tetrahydrate ($(NH_4)_6Mo_7O_{24} \cdot 4H_2O$, 99%), thiourea ($CH_4N_2S$, 99%), urea ($CO(NH_2)_2$), ammonium fluoride ($NH_4F$), ethylene glycol ($C_2H_6O_2$), glycerol ($C_3H_8O_3$, 99%) and potassium hydroxide were purchased from Shanghai Aladdin Reagent Co., Ltd and all reagents were analytical grade. Platinum carbon (Pt/C, 20%) and Iridium dioxide (IrO_2, 99.9%) were obtained from Suzhou Sinero Technology Co., Ltd. Nickel foam (NF) was bought by Kunshan Material Co., Ltd and pretreated by ultrasonication in 3 M hydrochloric acid and acetone solutions for 15 minutes each, followed by cleaning, drying, and storage for later use.

2.2 Synthesis of electrocatalysts

The Ni–Mo–S electrocatalyst was synthesized *via* a modified one-pot hydrothermal method based on a previously reported approach.[25] In brief, 2.50 g of $Ni(CH_3COO)_2 \cdot 4H_2O$, 1.77 g of $(NH_4)_6Mo_7O_{24} \cdot 4H_2O$, 1.52 g of CH_4N_2S, 0.60 g of $CO(NH_2)_2$ and 0.74 g of NH_4F were dissolved in 50 mL of a 20% ethylene glycol aqueous solution under ultrasonication and magnetic stirring. Then, two pieces of pre-treated nickel foam (1 cm × 1 cm) were cut and placed into the mixed solution, and the mixture was transferred into a 100 mL Teflon-lined autoclave. The autoclave was maintained at 160 °C for 8 hours. After cooling to room temperature, the electrode sheets were taken out and washed several times with deionized water, followed by freeze-drying to obtain the final electrocatalyst. For comparison, the Ni–Mo-Pre electrocatalyst was synthesized following the same protocol but without the addition of thiourea. Additionally, commercial Pt/C/nickel foam and IrO_2/nickel foam electrodes were prepared as reference electrodes according to previously reported methods in the literature.

The detailed electrocatalyst characterizations can be seen in the SI of Text S1.

2.3 Electrochemical measurements

All HER, OER, and GOR measurements were conducted in a standard three-electrode cell configuration using a CHI 760E electrochemical workstation,[25] where a carbon rod and Ag/AgCl (saturated KCl) served as the counter electrode and reference electrode, respectively. The measurements were carried out in 1.0 M KOH solution at room temperature, varying only in glycerol addition. Linear sweep voltammetry (LSV) curves were measured at a potential scan rate (v) of 10 mV s^{-1} and used without IR compensation. All potentials were calibrated against the reversible hydrogen electrode (RHE), calculated using eqn (1).

$$E_{RHE} = E_{Ag/AgCl} + 0.059\ pH + 0.195 \quad (1)$$

Electrochemical impedance spectroscopy (EIS) measurements were conducted using a 10 mV AC perturbation amplitude across the frequency range of 0.1–10^5 Hz. All electrochemical measurements were conducted in N_2-saturated electrolyte.

The theoretical H_2 yield was computed *via* eqn (2).

$$V_{H_2} = Q_{total} \times V_m/(n_1 \times F \times N_A) \quad (2)$$

where V_{H_2} represents the hydrogen production volume, Q_{total} is the total charge passed through the electrode, V_m denotes the molar volume of gas, $n_1 = 2$ corresponds to the number of electrons required to produce one H_2 molecule, N_A is the Avogadro constant, and $F = 96\,485$ C mol^{-1} stands for the Faraday constant.

The formate production yield (%) and selectivity (%) are determined by eqn (3) and (4).

$$\text{Yield (\%)} = C_{formate}/(3 \times C_{(glycerol)0}) \times 100\% \quad (3)$$

$$\text{Selectivity (\%)} = C_{formate}/(3 \times C_{(glycerol)x}) \times 100\% \quad (4)$$

The faradaic efficiencies (FE, %) for formate production and hydrogen evolution were quantified *via* eqn (5) and (6), correspondingly.

$$\text{FE (\%)} = n_2 \times F \times C_{formate} \times V_q/Q_{total} \quad (5)$$

$$\text{FE (\%)} = n_1 \times F \times N_A \times V_{H_2}/(Q_{total} \times V_m) \quad (6)$$

where $C_{formate}$ is the concentration of produced formate, $C_{(glycerol)0}$ and $C_{(glycerol)x}$ represent the initial glycerol concentration and consumed glycerol concentration, respectively, $n_2 = 8/3$ corresponds to the number of electrons required to produce one formate molecule, and V_q denotes the volume of the solution.

3. Results and discussion

3.1 Characterization of catalysts

The SEM images (Fig. 1a and b) reveal that the originally smooth nickel foam surface became uniformly covered with coral-like Ni–Mo–S nanostructures after the hydrothermal reaction. These structures consisted of densely packed branched nanorods with diameters of approximately 50–100 nm and lengths reaching 1–2 μm, exhibiting a radiating cluster morphology extending outward from the substrate, resembling the porous hierarchical structure of natural coral. Higher-magnification SEM image (Fig. 1c) further demonstrates that the nanorod surfaces were rough and contain numerous nanopores (5–20 nm in diameter), which significantly increased the material's specific surface area and provided abundant exposed active sites for catalytic reactions. Elemental mapping (Fig. 1d) *via* energy-dispersive X-ray spectroscopy (EDS) confirms the uniform spatial distribution of nickel, molybdenum, and sulfur constituents within the coralloid framework, with no detectable phase separation or elemental clustering. The experimentally determined stoichiometry (Ni : Mo : S = 1 : 0.8 : 2.3, Table S1) agrees well with the designed $NiMoS_x$ composition. Minor oxygen contamination (<5 at%) detected in localized regions likely originate from either surface partial oxidation or adsorbed species.

High-resolution TEM analysis (Fig. 1e) demonstrates distinct lattice spacings of 0.277 nm, 0.227 nm, and 0.203 nm, which are indexed to NiS (300), MoS_2 (103), and Ni (111) crystallographic planes, respectively, confirming the coexistence of both sulfide phases and metallic molybdenum in the nanostructure. The XRD pattern (Fig. 1f) shows diffraction peaks at $2\theta = 44.5°$, 51.8°, and 76.4° are attributed to the (111), (200), and (220) planes of the nickel foam substrate, respectively, which matched well with the standard JCPDS no. 04-0850 card. The intense peaks at $2\theta = 39.2°$, 50.1°, and 73.0°, corresponding to the (103), (105), and (203) planes of MoS_2 (JCPDS no. 02-1133 card), confirming the formation of layered MoS_2. Diffraction peaks at $2\theta = 31.0°$ is attributed to the (300) planes of the NiS lattice (JCPDS no. 03-0760 card). Diffraction peaks at $2\theta = 55.2°$ falls between the three compounds and may be attributed to their minimal coexistence. The above XRD analysis was consistent with the TEM results, further verifying the effective synthesis of the Ni–Mo–S/NF catalyst. Notably, the (300) diffraction peak exhibits a 0.6° shift toward higher angles, likely resulting from lattice shrinkage caused by Mo atom incorporation into the NiS lattice. Such lattice distortion could effectively modulate the electronic structure of the catalyst and enhance its adsorption capacity for reaction intermediates.

The XPS survey spectrum (Fig. S1) confirms the presence of Ni, Mo, S, and O elements in the catalyst. The atomic percentage of O is approximately 4.5%, which may originate from surface-adsorbed hydroxyl groups (–OH) or slight oxidation. The atomic ratios of Ni, Mo, and S, calculated by peak integration, are 1 : 0.92 : 2.15, close to the stoichiometric ratio of $NiMoS_x$, indicating a relatively pure phase composition of the catalyst. High-resolution XPS spectral deconvolution results reveal that the Ni 2p region exhibited characteristic peaks of divalent nickel (Ni^{2+}) and zerovalent nickel (Ni^0) (Fig. 2a). The Ni^{2+} $2p_{3/2}$ peak was located at 855.9 eV, with a satellite peak at 862.0 eV, while the Ni^0 peak appeared at ~852.3 eV ($2p_{3/2}$).[26,27] Quantitative analysis of peak areas indicated that Ni^{2+} accounted for ~83% of the total Ni 2p intensity, whereas Ni^0 contributed ~17%, reflecting the distribution of nickel chemical states on the catalyst surface. The presence of Ni^0 enhanced the electrical conductivity of the catalyst, providing efficient electron transport pathways for electrocatalytic reactions.[28] Meanwhile, Ni^{2+} likely participated in active site formation, where its synergistic interaction with neighboring atoms facilitated the adsorption and activation of reactant molecules, playing a critical role in redox processes. In the Mo 3d region (Fig. 2b), the characteristic peaks at 231.8 eV ($3d_{3/2}$) and 229.2 eV ($3d_{5/2}$) were assigned to Mo^{4+}, while the peak at 235.2 eV corresponds to Mo^{6+}.[29] The Mo^{4+}/Mo^{6+} ratio (~4 : 1) indicated that molybdenum primarily existed in a sulfided state (MoS_2), which was crucial for the hydrogen evolution reaction (HER).[30]

The presence of Mo^{6+} suggested the formation of a mixed Mo–S/O coordination environment in the catalyst. This unique configuration may facilitate adsorption of oxygen-containing

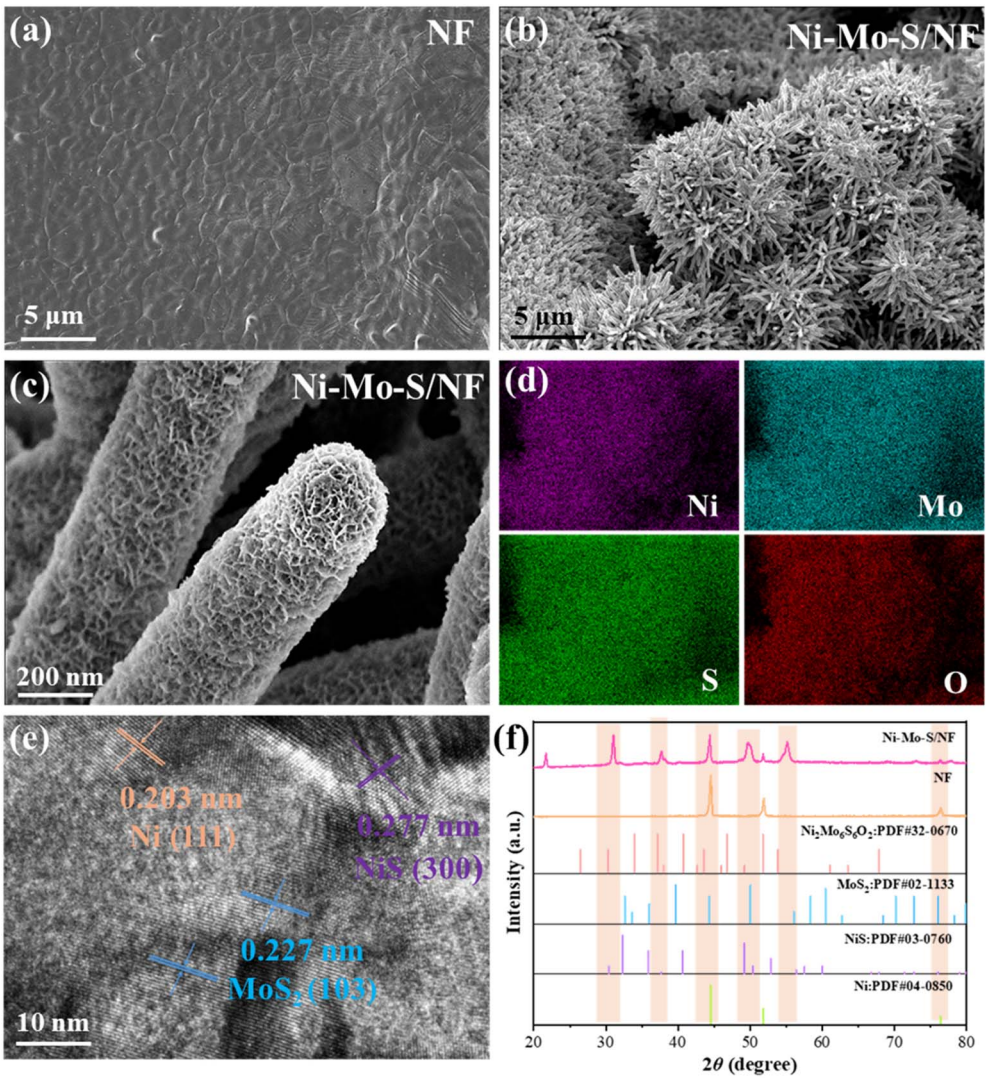

Fig. 1 (a–d) SEM-EDS patterns, (e) TEM pattern and (f) XRD patterns.

intermediates, conversion during redox processes and desorption of reaction products. These features collectively enhanced the catalyst's oxygen evolution activity. The synergistic effect between Mo^{4+} and Mo^{6+} species likely played a pivotal role in achieving bifunctional electrocatalytic performance for both HER and GOR.[31] In the S 2p region (Fig. 2c), the characteristic doublet at 163.3 eV ($2p_{3/2}$) and 164.5 eV ($2p_{1/2}$) corresponded to S^{2-} species (including Ni–S, and Mo–S bonds in respective sulfides).[32] The observation of a well-defined metal–sulfur (S^{2-}) spectral feature indicated that sulfur predominantly existed as metal sulfides in the catalyst. In the O 1s spectrum (Fig. 2d), the peaks at 529.7 eV and 531.3 eV were assigned to metal–oxygen bonds (M–O, M = Ni or Mo) and hydroxyl groups (OH^-), respectively.[33] The presence of OH^- groups suggested a hydrophilic surface, which facilitated electrolyte access during electrocatalysis, while M–O bonds may stabilize the catalyst structure.

3.2 Electrocatalytic performance for GOR

Building upon the morphological and compositional characterizations, the electrocatalytic performance of the Ni–Mo–S/NF anode for glycerol oxidation reaction (GOR) was systematically investigated in a standard three-electrode cell configuration using 1.0 M KOH electrolyte. Fig. 3a shows the linear sweep voltammetry (LSV) curves of Ni–Mo–S/NF in the electrolyte system with and without glycerol. In the absence of glycerol, the electrode exhibited moderate OER activity, achieving an anodic current density of 10 mA cm^{-2} at a potential of 1.59 V *versus* the reversible hydrogen electrode (*vs.* RHE). The peak center of OER at approximately 1.42 V *vs.* RHE may be attributed to the oxidation peak of Ni^{2+}/Ni^{3+}. Upon the introduction of 0.1 M glycerol, the current density increased significantly, and the anodic potential at 10 mA cm^{-2} decreased markedly to 1.31 V *vs.* RHE. For further comparison, the potentials at different current densities were obtained from the LSV curves, as shown in Fig. 3b. Compared to the OER, the addition of 0.1 M glycerol reduced the anodic potential by 250–350 mV at current densities of 10, 20, 50, 100, and 150 mA cm^{-2}. This significantly lowered energy consumption, with the overpotential being lower than that of most reported electrochemically assisted water-splitting systems.[34] Furthermore, the Tafel slope of the

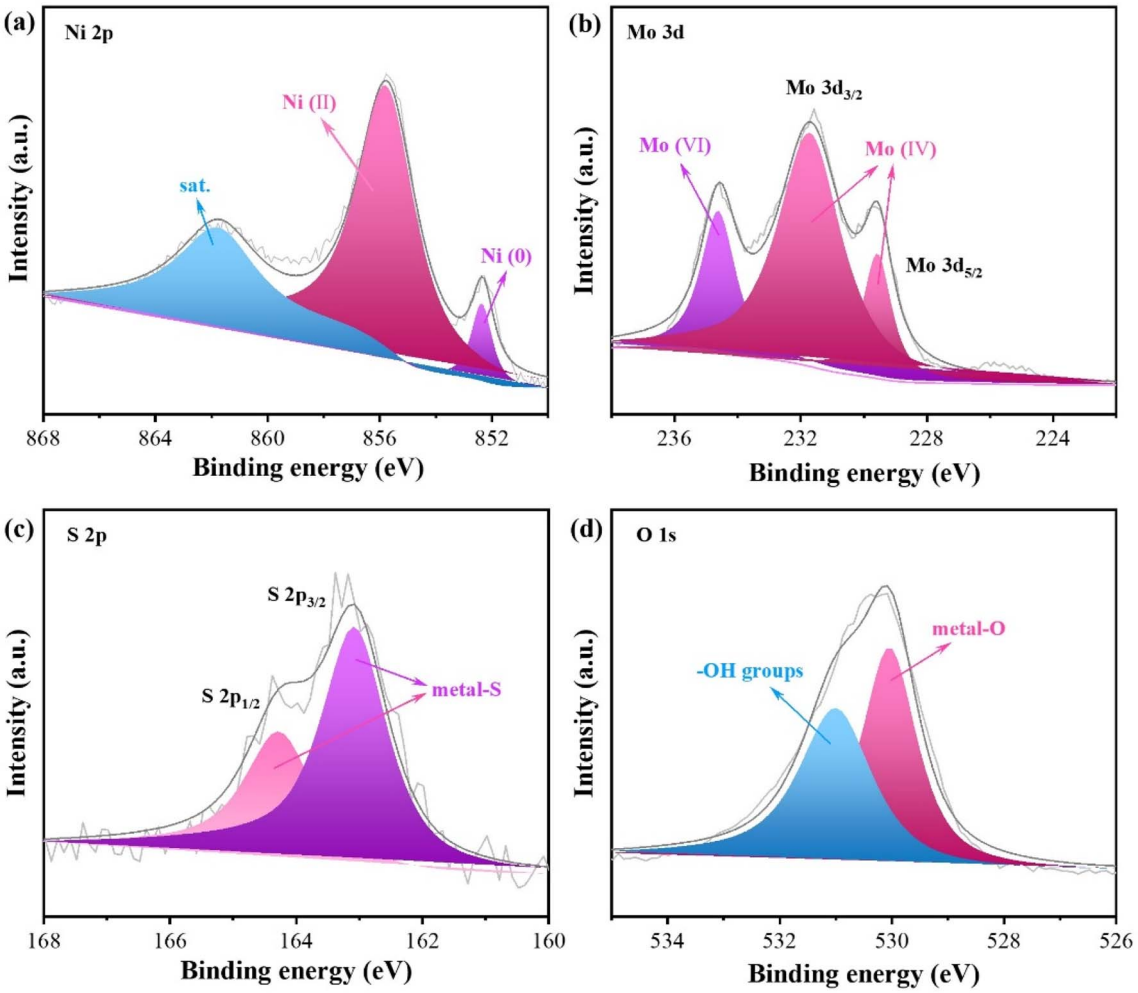

Fig. 2 High-resolution XPS survey of (a) Ni 2p, (b) Mo 3d, (c) S 2p and (d) O 1s.

catalyst can serve as an effective indicator for investigating the underlying reaction mechanism of electro-oxidation from a kinetic perspective. As derived from the LSV data and shown in Fig. 3c, the Ni–Mo–S/NF exhibited a remarkably low Tafel slope of only 93 mV dec^{-1} for glycerol oxidation, which was significantly lower than the 187 mV dec^{-1} observed for the OER. This clearly demonstrated that the catalytic kinetics of glycerol oxidation reaction (GOR) were substantially faster. Since glycerol concentration significantly affects the electrooxidation performance, SI Fig. S2 presents the LSV curves of the anode within a glycerol concentration range of 0.01–0.2 M. The results demonstrated that the anode exhibited optimal electrooxidation activity in the electrolyte containing 0.1 M glycerol. Excessive glycerol concentrations showed adverse effects, likely due to reduced solution conductivity.[35]

For comparison, the benchmark electrocatalytic activities of Ni–Mo-Pre/NF, bare NF, and pristine IrO_2/NF were evaluated under identical experimental conditions in a 1.0 M KOH electrolyte containing 0.1 M glycerol. The LSV curves (Fig. 3d) demonstrate that Ni–Mo–S/NF exhibited significantly stronger glycerol electrooxidation performance than other anode catalysts, while its corresponding Tafel slope was the lowest (Fig. 3e), indicating the fastest reaction kinetics. Furthermore, electrochemical impedance spectroscopy (EIS) in Fig. 3f reveals that Ni–Mo–S/NF exhibited a significantly lower charge transfer resistance compared to Ni–Mo-Pre/NF and NF electrodes, indicating its excellent electrical contact, extremely low impedance, and rapid charge transfer rate.

The electrode potential has a direct and significant impact on the selectivity of glycerol electrooxidation products and Faraday efficiency. Through quantitative analysis of formic acid production at different potentials using nuclear magnetic resonance (NMR) spectroscopy, the potential with optimal energy efficiency was determined. Faradaic efficiency and selectivity of formic acid initially increased and then decreased with rising electrode potential (Fig. 4a). This was because at lower potential, C–C bond cleavage remained incomplete, while at higher potential, the oxygen evolution reaction competed with glycerol oxidation. Therefore, a potential of ~1.35 V was identified as the optimal energy efficiency potential, at which the formate selectivity and faradaic efficiency can reach as high as ~86% and ~95%, respectively. The ^{1}H NMR spectra (Fig. S3)

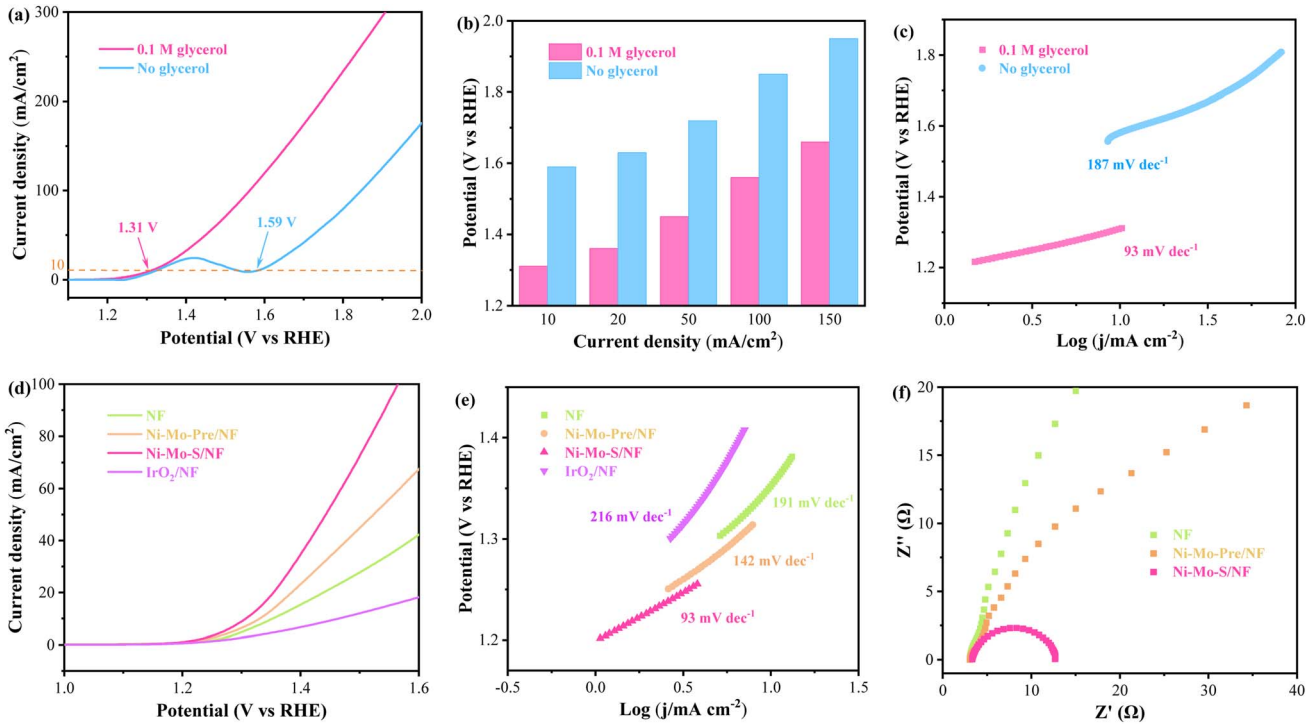

Fig. 3 (a) LSV curves of Ni–Mo–S/NF anode with and without 0.1 M glycerol, (b) comparisons of the anodic potentials on varied current densities, (c) Tafel plots for the anodic GOR or OER derived from (a), (d) comparisons of the GOR activities among various catalysts and (e) their corresponding Tafel slopes, (f) Nyquist plots of catalysts for electrochemical impedance spectroscopy (EIS) analyses.

of glycerol oxidation products showed no detectable carbon-containing products other than formate. While the ^{13}C NMR spectra (Fig. S4) could identify both formate and carbonate, the faradaic efficiency of carbonate was remarkably low (<~3%), rendering it virtually negligible. Calculations demonstrated that the overall system exhibited an electron transfer-to-formate molar ratio of 2.69 : 1 to 2.80 : 1, closely approximating the theoretical 8 : 3 ratio. This corresponded to the production of 3 moles of formate per mole of glycerol consumed, indicating that the Ni–Mo–S/NF electrode displayed exceptional selectivity toward formate production through glycerol electrooxidation.

Stability serves as a crucial metric for evaluating catalyst performance and application potential. Continuous glycerol electrooxidation tests over 10 cycles demonstrated that the faradaic efficiency for formate production consistently remained high at 90–96% (Fig. 4b). Furthermore, the electrochemical stability of the Ni–Mo–S/NF electrode during glycerol oxidation was evaluated by monitoring the potential–time (U–t) curve. As shown in Fig. 4c, no significant potential increase was observed during the 25-hour stability test (with merely a 0.06 V potential rise, representing less than 2% change), demonstrating excellent stability of the anode catalyst.

3.3 HER of catalyst

In alkaline electrolyte, the Ni–Mo–S/NF electrode also demonstrated outstanding HER performance as a cathode. As

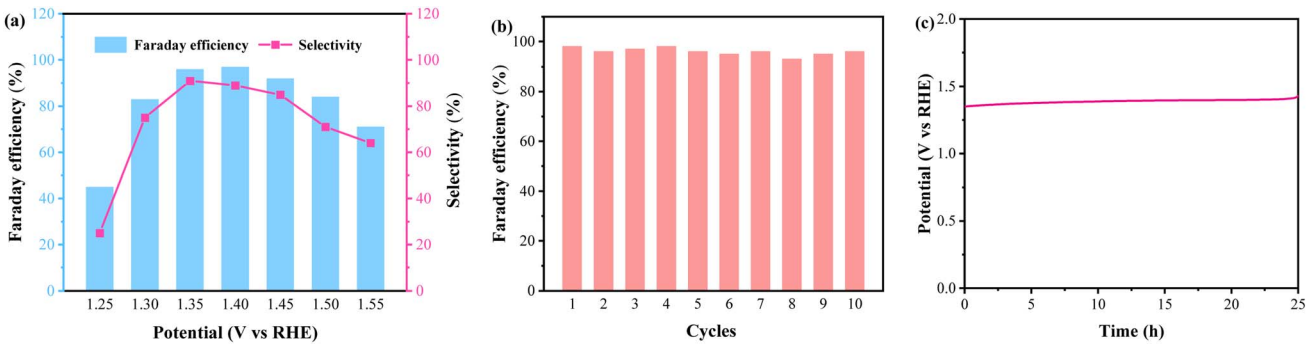

Fig. 4 (a) Faradaic efficiencies (FEs) and selectivity for formate production at varied potentials, (b) FEs of Ni–Mo–S/NF for formate production for 10 electrolysis cycles, and (c) 25-hour stability test of Ni–Mo–S/NF for the anodic glycerol oxidation at a current density of 10 mA cm^{-2}.

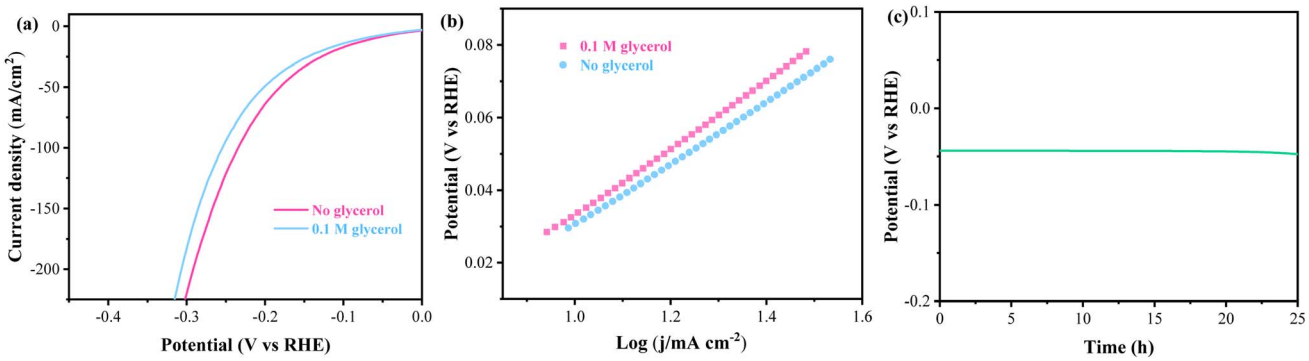

Fig. 5 (a) LSV curves of Ni–Mo–S/NF cathode with and without 0.1 M glycerol, (b) their corresponding Tafel slopes, (c) 25-hour stability test of Ni–Mo–S/NF for the cathodic HER at a current density of 10 mA cm^{-2}.

illustrated in Fig. S5a, Ni–Mo–S/NF required merely 58 mV overpotential to drive the HER at a current density of 10 mA cm^{-2}, significantly lower than those of NF (274 mV) and Ni–Mo-Pre/NF (192 mV). Additionally, the Ni–Mo–S/NF catalyst exhibited a remarkably low Tafel slope of 76 mV dec^{-1}, which was comparable to the noble metal catalyst Pt/C/NF (69 mV dec^{-1}) and substantially lower than those of Ni–Mo-Pre/NF (168 mV dec^{-1}) and NF (174 mV dec^{-1}) (Fig. S5b). This demonstrated the favorable HER kinetics of Ni–Mo–S/NF. The EIS analysis in Fig. S6 reveals that Ni–Mo–S/NF possessed the smallest charge transfer resistance, which was significantly lower than those of other electrodes, thereby greatly facilitating the enhancement of its catalytic activity.[36] To assess potential impacts of organic compounds like glycerol on HER performance in electrolytes, we evaluated the HER activity of Ni–Mo–S/NF with and without glycerol. The LSV curves in Fig. 5a demonstrate that the HER performance of the electrode in glycerol-containing electrolyte was minimally affected, with no significant change in Tafel slope (Fig. 5b). This indicated that Ni–Mo–S/NF not only exhibited excellent hydrogen evolution activity with fast reaction kinetics but also showed remarkable tolerance in the presence of glycerol. Furthermore, stability tests conducted at a constant current density of 10 mA cm^{-2} revealed that Ni–Mo–S/NF maintained its outstanding HER catalytic performance even after 25 hours of continuous operation (Fig. 5c).

3.4 Mechanism investigation

At room temperature, an electrolysis system capable of co-producing hydrogen and formate was constructed using Ni–Mo–S/NF as both the anode and cathode catalyst in a solution containing 0.1 mol L^{-1} glycerol and 1 mol L^{-1} KOH (denoted as Ni–Mo–S/NF ‖ Ni–Mo–S/NF), as illustrated in Fig. 6a. This system required only a low voltage of 1.37 V to achieve a current density of 10 mA cm^{-2}, demonstrating excellent co-electrolysis performance in both the hydrogen evolution reaction (HER) and glycerol oxidation. In contrast, a Ni–Mo–S/NF‖Ni–Mo–S/NF electrolyzer using an electrolyte without glycerol required a higher voltage (1.65 V) to reach the same current density under identical conditions (Fig. 6b). The chemical-assisted water electrolysis system for hydrogen production, constructed with Ni–Mo–S/NF as the electrocatalyst, operated at a significantly lower cell voltage than most reported systems,[37,38] representing a novel approach to electrolytic hydrogen production. Furthermore, as shown in Fig. 6c, this electrolyzer maintained excellent catalytic performance and charge selectivity even after prolonged operation. Under an applied voltage of 1.4 V (where competing water oxidation was negligible), the average faradaic efficiency for $HCOO^-$ production reached as high as 95.0%. Correspondingly, the experimentally measured hydrogen evolution matched well with the theoretical value (Fig. 6d), with a faradaic efficiency of 99.6% for the HER. These results demonstrated that the constructed glycerol oxidation/hydrogen evolution co-electrolysis system exhibited both high activity and remarkable durability.

To further investigate the stability and catalytic mechanism of the dual-electrode system for glycerol electrooxidation to formate and simultaneous low-energy hydrogen production, various characterizations were performed on the post-reaction Ni–Mo–S/NF catalyst. As shown in Fig. S7a, the high-resolution Ni $2p_{3/2}$ XPS spectrum of the post-reaction Ni–Mo–S/NF anode exhibited a noticeable enhancement at 856.5 eV. This indicated that most of the Ni(0) and/or Ni(II) species were oxidized to NiOOH. NiOOH has been reported as an active species for glycerol electrooxidation.[39,40] Correspondingly, the peak deconvolution analysis of the O 1s spectrum (Fig. S7b) reveals that the Ni–Mo–S/NF catalyst exhibited a higher concentration of –OH species (531.6 eV) after the reaction compared to its pre-reaction state. This observation may be attributed to the substitution of surface oxygen atoms, which facilitated the formation of NiOOH.[33] The Mo 3d XPS spectra (Fig. S7c) reveals a weakened signal intensity of Mo species after the reaction, indicating partial loss of Mo during the electrocatalytic oxidation process. Furthermore, a significant portion of Mo^{4+} was oxidized to Mo^{6+}. Furthermore, the corresponding SEM image (Fig. S7e) reveal that the Ni–Mo–S/NF maintained its coral-like morphology with minimal structural changes. However, XRD patterns demonstrate a significant attenuation of Mo species signals (Fig. S7d), suggesting possible structural transformation or leaching during the reaction process. The stability tests and cycling experiments of glycerol

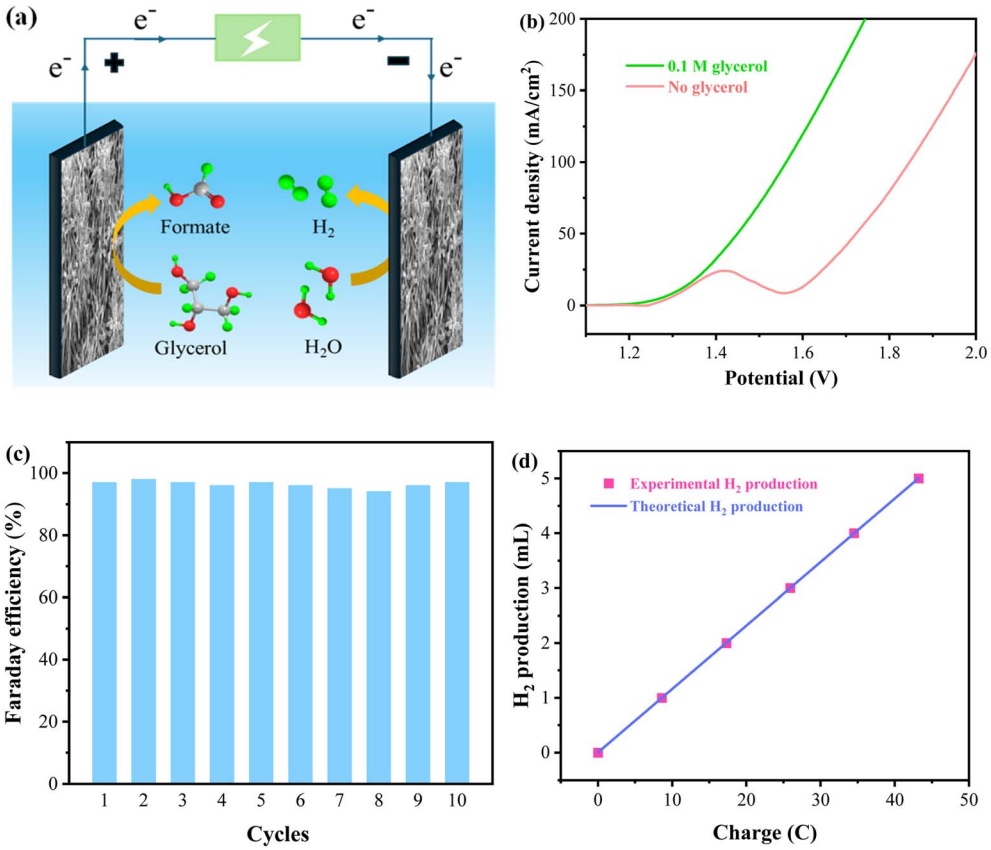

Fig. 6 (a) Schematic diagram of simultaneous production of formate and hydrogen by electro oxidation of glycerol, (b) LSV curves of Ni–Mo–S/NF||Ni–Mo–S/NF system with and without 0.1 M glycerol, (c) FEs of Ni–Mo–S/NF||Ni–Mo–S/NF system for formate production for 10 electrolysis cycles, (d) theoretical calculation and experimental measurement of hydrogen evolution.

electrooxidation revealed that despite significant Mo species leaching during the process, the catalyst maintained high stability and oxidation efficiency with negligible performance degradation. This observation suggested that Mo species may not directly participate in glycerol oxidation and were unlikely to serve as active sites in this work.

Simultaneously, XPS analysis of the Ni–Mo–S/NF cathode after the HER revealed that the oxidation state of Mo remained essentially unchanged (Fig. S8a), while the content of S existing as metal–S species showed only a slight decrease (Fig. S8b). This suggested minimal Mo species leaching at the cathode, which may be attributed to the inherent instability of Mo^{6+} species that readily dissolve as molybdate in alkaline electrolytes, while exhibiting significantly improved stability in reduced states like Mo^{4+}. The high-resolution Ni $2p_{3/2}$ spectrum (Fig. S8c) demonstrated that most Ni(0) had transformed into Ni(II), likely due to surface oxidation caused by either water vapor or dissolved oxygen in the electrolyte.[41] Notably, such Ni(II) species have been previously confirmed as active sites for hydrogen evolution through water splitting.[42,43] Subsequent characterization revealed that the coral-like morphology of the cathodic Ni–Mo–S/NF was well preserved, as evidenced by SEM image (Fig. S8e), while XRD patterns indicated no significant changes in its crystalline structure (Fig. S8d). These results provided a comprehensive explanation for the outstanding electrocatalytic performance and stability of the bifunctional Ni–Mo–S/NF catalyst in both electrooxidation and HER processes.

4. Conclusions

In summary, this study synthesized a novel nickel–molybdenum sulfide/nickel foam (Ni–Mo–S/NF) bifunctional electrocatalyst and constructed a two-electrode system using it as both the anode and cathode, achieving simultaneous and efficient production of formate and hydrogen in an alkaline glycerol electrolyte. The catalyst exhibited outstanding electrocatalytic performance in both roles, requiring only 1.31 V (anode) and 58 mV (cathode) to deliver a current density of 10 mA cm^{-2}. Furthermore, owing to the lower redox potential of glycerol compared to water, the alkaline glycerol electrolyzer in the two-electrode system required just 1.37 V to reach 10 mA cm^{-2}, which was 280 mV lower than conventional water splitting, corresponding to a 17% reduction in energy consumption. This bifunctional electrocatalytic system also enabled the highly selective upgrading of glycerol into formate, with faradaic efficiencies reaching 95.0% for formate production and 99.6% for hydrogen evolution. Additionally, chronoamperometry and cycling tests confirmed the catalyst's excellent long-term stability. By employing the non-precious Ni–Mo–S/NF bifunctional electrocatalyst, this work realized both the valorization of glycerol and energy-saving hydrogen production,

offering a new strategy for efficient formate synthesis and low-cost hydrogen generation.

Author contributions

Yong Liu: experiment, methodology, writing – original draft preparation. Bohong Chen: methodology, validation. Hanbin Nie: methodology, writing – reviewing and editing. Shuanglin Gui: validation, resources, conceptualization. Jianping Deng: writing – reviewing and editing, supervision, funding acquisition.

Conflicts of interest

The authors declare that they have no known competing financial interests or personal relationships that could have appeared to influence the work reported in this paper.

Data availability

The supporting data has been provided as part of the supplementary information (SI). Supplementary information is available. See DOI: https://doi.org/10.1039/d5ra08754f.

Acknowledgements

The authors thank the support from Key Research and Development Program of Jiangxi Province (20252BCG330019), Introduction of Doctor Program of Jiangxi Academy of Sciences (2024YYB17), Major Project for the Construction of Platform of Jiangxi Academy of Sciences (2024TJPT003).

References

1 S. R. W. Alwi, J. J. Klemes and P. S. Varbanov, Cleaner energy planning, management and technologies: perspectives of supply-demand side and end-of-pipe management, *J. Cleaner Prod.*, 2016, **136**, 1–13, DOI: 10.1016/j.jclepro.2016.07.181.

2 K. S. Gabriel, R. S. El-Emam and C. Zamfirescu, Technoeconomics of large-scale clean hydrogen production – a review, *Int. J. Hydrogen Energy*, 2022, **47**(72), 30788–30798, DOI: 10.1016/j.ijhydene.2021.10.081.

3 Z.-J. Zhang, H.-M. Xu, C.-J. Huang, T.-Y. Shuai, Q.-N. Zhan and G.-R. Li, Recent advances in the synthesis of transition metal hydroxyl oxide catalysts and their application in electrocatalytic oxygen evolution reactions, *Nanoscale*, 2024, **16**(43), 19970–19997, DOI: 10.1039/d4nr02400a.

4 Z. Feng, C. Dai, P. Shi, X. Lei, R. Guo, B. Wang, X. Liu and J. You, Seven mechanisms of oxygen evolution reaction proposed recently: a mini review, *Chem. Eng. J.*, 2024, **485**, 149992, DOI: 10.1016/j.cej.2024.149992.

5 X. Wen, NiFe-LDH/MWCNTs/NF nanohybrids as a high-performance bifunctional electrocatalyst for overall urea electrolysis, *Int. J. Hydrogen Energy*, 2020, **45**(29), 14660–14668, DOI: 10.1016/j.ijhydene.2020.03.192.

6 S. Hu, Y. Tan, C. Feng, H. Wu, J. Zhang and H. Mei, Synthesis of N doped NiZnCu-layered double hydroxides with reduced graphene oxide on nickel foam as versatile electrocatalysts for hydrogen production in hybrid-water electrolysis, *J. Power Sources*, 2020, **453**, 227872, DOI: 10.1016/j.jpowsour.2020.227872.

7 Z. Hu, J. Wu, Z. He, Y. Zhang, Y. Li, Q. Peng and S. Wu, Mechanism and model of current response of hydroxylamine nitrate-based energetic polymer electrolytes under high voltage, *Chem. Eng. J.*, 2025, **510**, 161628, DOI: 10.1016/j.cej.2025.161628.

8 W. Kang, L. Li, Q. Zhao, C. Wang, J. Wang and Y. Teng, Application of New Hydrogen and Oxygen Evolution Electrochemical Catalysts for Solid Polymer Water Electrolysis System, *Prog. Chem.*, 2020, **32**(12), 1952–1977, DOI: 10.7536/pc200319.

9 R. Hu, C. Wen, Z. Ye, Y. Qi, B. Zhang, K. Kang, Y. Gao, D. Wang and Z. Tu, A comprehensive review of flow channel designs and optimizations for water electrolysis technology, *Appl. Energy*, 2025, **400**, 126643, DOI: 10.1016/j.apenergy.2025.126643.

10 Z. Chen, W. Wei, H. K. Shon and B.-J. Ni, Designing bifunctional catalysts for urea electrolysis: progress and perspectives, *Green Chem.*, 2024, **26**(2), 631–654, DOI: 10.1039/d3gc03329e.

11 M. Kumar, B. Meena, A. Yu, C. Sun and S. Challapalli, Advancements in catalysts for glycerol oxidation *via* photo-/electrocatalysis: a comprehensive review of recent developments, *Green Chem.*, 2023, **25**(21), 8411–8443, DOI: 10.1039/d3gc03094f.

12 X. Hu, J. Lu, Y. Liu, L. Chen, X. Zhang and H. Wang, Sustainable catalytic oxidation of glycerol: a review, *Environ. Chem. Lett.*, 2023, **21**(5), 2825–2861, DOI: 10.1007/s10311-023-01608-z.

13 H. Luo, J. Barrio, N. Sunny, A. Li, L. Steier, N. Shah, I. E. L. Stephens and M.-M. Titirici, Progress and Perspectives in Photo- and Electrochemical-Oxidation of Biomass for Sustainable Chemicals and Hydrogen Production, *Adv. Energy Mater.*, 2021, **11**(43), 2101180, DOI: 10.1002/aenm.202101180.

14 R. Li, K. Xiang, Z. Peng, Y. Zou and S. Wang, Recent Advances on Electrolysis for Simultaneous Generation of Valuable Chemicals at Both Anode and Cathode, *Adv. Energy Mater.*, 2021, **11**(46), 2102292, DOI: 10.1002/aenm.202102292.

15 S. Ghosh, D. Bagchi, I. Mondal, T. Sontheimer, R. V. Jagadeesh and P. W. Menezes, Deciphering the Role of Nickel in Electrochemical Organic Oxidation Reactions, *Adv. Energy Mater.*, 2024, **14**(22), 2400696, DOI: 10.1002/aenm.202400696.

16 N. Heidary and N. Kornienko, *Operando*vibrational spectroscopy for electrochemical biomass valorization, *Chem. Commun.*, 2020, **56**(62), 8726–8734, DOI: 10.1039/d0cc03084h.

17 F. Wang, L. Xiao, Y. Jiang, X. Liu, X. Zhao, Q. Kong, A. Abdukayum and G. Hu, Recent achievements in noble metal-based oxide electrocatalysts for water splitting,

Mater. Horiz., 2025, **12**(6), 1757–1795, DOI: 10.1039/d4mh01315h.

18 R. Song, X. Wang and J. Ge, Recent progress of noble metal-based single-atom electrocatalysts for acidic oxygen evolution reaction, *Curr. Opin. Electrochem.*, 2023, **42**, 101379, DOI: 10.1016/j.coelec.2023.101379.

19 H. Wu, C. Feng, L. Zhang, J. Zhang and D. P. Wilkinson, Non-noble Metal Electrocatalysts for the Hydrogen Evolution Reaction in Water Electrolysis, *Electrochem. Energy Rev.*, 2021, **4**(3), 473–507, DOI: 10.1007/s41918-020-00086-z.

20 D. Tan, H. Xiong, T. Zhang, X. Fan, J. Wang and F. Xu, Recent progress in noble-metal-free electrocatalysts for alkaline oxygen evolution reaction, *Front. Chem.*, 2022, **10**, 1071274, DOI: 10.3389/fchem.2022.1071274.

21 J. Wang, F. Xu, H. Jin, Y. Chen and Y. Wang, Non-noble Metal-Based Carbon Composites in Hydrogen Evolution Reaction: Fundamentals to Applications, *Adv. Mater.*, 2017, **29**(14), 1605838, DOI: 10.1002/adma.201605838.

22 W. Bi, Q. Zhou, Y. Sun, J. Wan, S. Xie, Y. Hou, M. Yu, T. Li, J. Lian and B. Liu, Enhancement of hydrogen evolution activity of CoS_2/MoS_2 heterostructure catalysts by electronic structure modulation, *J. Alloys Compd.*, 2024, **1005**, 175847, DOI: 10.1016/j.jallcom.2024.175847.

23 Z. Xue, X. Li, Q. Liu, M. Cai, K. Liu, M. Liu, Z. Ke, X. Liu and G. Li, Interfacial Electronic Structure Modulation of NiTe Nanoarrays with NiS Nanodots Facilitates Electrocatalytic Oxygen Evolution, *Adv. Mater.*, 2019, **31**(21), 1900430, DOI: 10.1002/adma.201900430.

24 W. Liu, F. Wang, A. Wang, Y. Guo, H. Yin and D. Wang, Boosting Alkaline Hydrogen Evolution Reaction by Modulating D-Band Center in Bimetallic Sulfide Ni_3S_2–FeS Heterointerfaces, *Small*, 2025, **21**(5), 2411028, DOI: 10.1002/smll.202411028.

25 Y. Li, X. Wei, L. Chen, J. Shi and M. He, Nickel–molybdenum nitride nanoplate electrocatalysts for concurrent electrolytic hydrogen and formate productions, *Nat. Commun.*, 2019, **10**, 5335, DOI: 10.1038/s41467-019-13375-z.

26 T. Wang, X. Wang, Y. Liu, J. Zheng and X. Li, A highly efficient and stable biphasic nanocrystalline Ni–Mo–N catalyst for hydrogen evolution in both acidic and alkaline electrolytes, *Nano Energy*, 2016, **22**, 111–119, DOI: 10.1016/j.nanoen.2016.02.023.

27 B. Chang, J. Yang, Y. Shao, L. Zhang, W. Fan, B. Huang, Y. Wu and X. Hao, Bimetallic NiMoN Nanowires with a Preferential Reactive Facet: An Ultraefficient Bifunctional Electrocatalyst for Overall Water Splitting, *ChemSusChem*, 2018, **11**(18), 3198–3207, DOI: 10.1002/cssc.201801337.

28 Q. Wang, X. Zhou, H. Jin, L. Guo, Y. Wu and S. Ren, Cu-doped Ni_3S_2 electrocatalyst for glycerol oxidation coupling to promote hydrogen evolution reaction, *Fuel*, 2024, **377**, 132770, DOI: 10.1016/j.fuel.2024.132770.

29 A. Wu, Y. Xie, H. Ma, C. Tian, Y. Gu, H. Yan, X. Zhang, G. Yang and H. Fu, Integrating the active OER and HER components as the heterostructures for the efficient overall water splitting, *Nano Energy*, 2018, **44**, 353–363, DOI: 10.1016/j.nanoen.2017.11.045.

30 Y. Liu, X. Luo, C. Zhou, S. Du, D. Zhen, B. Chen, J. Li, Q. Wu, Y. Iru and D. Chen, A modulated electronic state strategy designed to integrate active HER and OER components as hybrid heterostructures for efficient overall water splitting, *Appl. Catal., B*, 2020, **260**, 118197, DOI: 10.1016/j.apcatb.2019.118197.

31 Y. Wang, Y. Sun, F. Yan, C. Zhu, P. Gao, X. Zhang and Y. Chen, Self-supported NiMo-based nanowire arrays as bifunctional electrocatalysts for full water splitting, *J. Mater. Chem. A*, 2018, **6**(18), 8479–8487, DOI: 10.1039/c8ta00517f.

32 D. Li, W. Wan, Z. Wang, H. Wu, S. Wu, T. Jiang, G. Cai, C. Jiang and F. Ren, Self-Derivation and Surface Reconstruction of Fe-Doped Ni_3S_2 Electrode Realizing High-Efficient and Stable Overall Water and Urea Electrolysis, *Adv. Energy Mater.*, 2022, **12**(39), 2201913, DOI: 10.1002/aenm.202201913.

33 P. W. Menezes, A. Indra, C. Das, C. Walter, C. Goebel, V. Gutkin, D. Schmeisser and M. Driess, Uncovering the Nature of Active Species of Nickel Phosphide Catalysts in High-Performance Electrochemical Overall Water Splitting, *ACS Catal.*, 2017, **7**(1), 103–109, DOI: 10.1021/acscatal.6b02666.

34 A. Li, Z. Qiliang, Y. Mi, H. U. Rehman, M. Shoaib, X. Cao and N. Wang, Triboelectric Nanogenerator Drives Electrochemical Water Splitting for Hydrogen Production: Fundamentals, Progress, and Challenges, *Small*, 2025, **21**(1), 2407043, DOI: 10.1002/smll.202407043.

35 X. Huang, M. Wang, H. Zhong, X. Li, H. Wang, Y. Lu, G. Zhang, Y. Liu, P. Zhang, R. Zou, *et al.*, Metal-Phthalocyanine-Based Two-Dimensional Conjugated Metal–Organic Frameworks for Electrochemical Glycerol Oxidation Reaction, *Angew. Chem., Int. Ed.*, 2025, **64**(4), e202416178, DOI: 10.1002/anie.202416178.

36 J. Jana, T. S. K. Sharma, M. A. Ghanem, W. M. Choi, C. S. Gopinath and S. H. Hur, Europium oxide on carbon nitride for electrocatalytic glycerol oxidation coupled with hydrogen evolution reaction, *Sep. Purif. Technol.*, 2025, **372**, 133442, DOI: 10.1016/j.seppur.2025.133442.

37 S. Chen, W. Zhou, Y. Ding, G.-B. Zhao and J. Gao, Communication-Oxalic Acid Assisted Water Electrolysis for Less Energy-Intensive Electrochemical Hydrogen Production, *J. Electrochem. Soc.*, 2020, **167**(13), DOI: 10.1149/1945-7111/abb70a.

38 G. Feng, Y. Pan, D. Su and D. Xia, Constructing Fully-Active and Ultra-Active Sites in High-Entropy Alloy Nanoclusters for Hydrazine Oxidation-Assisted Electrolytic Hydrogen Production, *Adv. Mater.*, 2024, **36**(13), 2309715, DOI: 10.1002/adma.202309715.

39 V. L. Oliveira, C. Morais, K. Servat, T. W. Napporn, G. Tremiliosi-Filho and K. B. Kokoh, Studies of the reaction products resulted from glycerol electrooxidation on Ni-based materials in alkaline medium, *Electrochim. Acta*, 2014, **117**, 255–262, DOI: 10.1016/j.electacta.2013.11.127.

40 R. M. A. Tehrani and S. Ab Ghani, Electrocatalysis of free glycerol at a nanonickel modified graphite electrode and

its determination in biodiesel, *Electrochim. Acta*, 2012, **70**, 153–157, DOI: 10.1016/j.electacta.2012.03.044.

41 H. Zhang, Y. Wang, X. Li, K. Deng, H. Yu, Y. Xu, H. Wang, Z. Wang and L. Wang, Electrocatalytic upcycling of polyethylene terephthalate plastic to formic acid coupled with energy-saving hydrogen production over hierarchical Pd-doped NiTe nanoarrays, *Appl. Catal. B: Environ. Energy*, 2024, **340**, 123236, DOI: 10.1016/j.apcatb.2023.123236.

42 Z.-Y. Yu, Y. Duan, M.-R. Gao, C.-C. Lang, Y.-R. Zheng and S.-H. Yu, A one-dimensional porous carbon-supported Ni/Mo_2C dual catalyst for efficient water splitting, *Chem. Sci.*, 2017, **8**(2), 968–973, DOI: 10.1039/c6sc03356c.

43 M. Gong, W. Zhou, M. J. Kenney, R. Kapusta, S. Cowley, Y. Wu, B. Lu, M.-C. Lin, D.-Y. Wang, J. Yang, *et al.*, Blending Cr_2O_3 into a NiO–Ni Electrocatalyst for Sustained Water Splitting, *Angew. Chem., Int. Ed.*, 2015, **54**(41), 11989–11993, DOI: 10.1002/anie.201504815.